

# Molecular Dynamics Study of Hydration in Ethanol–Water Mixtures Using a Polarizable Force Field<sup>†</sup>

Sergei Yu. Noskov,<sup>‡,§</sup> Guillaume Lamoureux,<sup>‡,||</sup> and Benoît Roux<sup>\*,‡</sup>

Department of Biochemistry, Weill Medical College of Cornell University, 1300 York Avenue, New York, New York 10021, and Département de physique, Université de Montréal, C.P. 6128, succ. centre-ville, Montréal, Québec H3C3J7, Canada

Received: October 6, 2004; In Final Form: November 29, 2004

The abnormal physicochemical characteristics of ethanol solvation in water are commonly attributed to the phenomenon of hydrophobic hydration. To investigate the structural organization of hydrophobic hydration in water–ethanol mixtures, we use molecular dynamics simulations based on detailed atomic models. Induced polarization is incorporated into the potential function on the basis of the classical Drude oscillator model. Water–ethanol mixtures are simulated at 11 ethanol molar fractions, from 0.05 to 0.9. Although the water and ethanol models are parametrized separately to reproduce the vaporization enthalpy, static dielectric constant, and self-diffusion constant of neat liquids at ambient conditions, they also reproduce the energetic and dynamical properties of the mixtures accurately. Furthermore, the calculated dielectric constant for the various water–alcohol mixtures is in excellent agreement with experimental data. The simulations provide a detailed structural characterization of the mixtures. A depletion of water–water hydrogen bonding in the first hydration shell of ethanol is compensated by an enhancement in the second hydration shell. The structuring effect from the second solvation shell gives rise to a net positive hydrogen-bonding excess for ethanol molar fractions up to  $\approx 0.5$ . For larger molar fractions, the second hydration shell is not sufficiently populated to overcome the net H-bond depletion from the first shell.

## Introduction

Solvation of polar and nonpolar moieties in liquid water is one of the key factors that governs the structural stability of proteins. Despite the great importance of hydrophobic hydration, many of its aspects are not completely understood.<sup>1–3</sup> From this point of view, the solvation of alcohols in liquid water provides perhaps the most elementary but nontrivial model system in which hydration of nonpolar and polar hydrogen-bonding groups are directly and intimately competing. Hydration of alcohols is commonly interpreted structurally in terms of the classical “iceberg” picture of Frank and Evans.<sup>4</sup> Within this framework, it has been suggested that the water molecules surrounding a nonpolar moiety are rearranging into a low-entropy cage with stronger hydrogen bonds (H-bonds). Although there is broad support for this view,<sup>5–7,15</sup> a different perspective is suggested by recent scattering measurements<sup>8–10</sup> as well as molecular dynamics (MD) simulations.<sup>11–13</sup> Studies combining diffraction data with computations by Soper et al.<sup>70</sup> found that there are only minor changes in H-bond occurrence in the first hydration shell of hydrated alcohols but that there is a higher solvent density (“compaction”) in the second hydration shell. These results suggest that the structural complexity of alcohol–water mixtures may, in fact, extend well beyond a simple picture based on the first solvation shell. Numerous experimental evidence collected from compressibility, UV and IR absorption spectra,<sup>14</sup> dielectric relaxation and Raman spectra investigations,<sup>15</sup> and

neutron scattering studies<sup>9,20</sup> indicate that there is a competition between formation of solute–solute, solvent–solvent, and solute–solvent clusters. The nature of these structural rearrangements is not completely understood.<sup>9,15</sup> Monatomic alcohols may be considered as the simplest molecular solute simultaneously presenting hydrophobic and hydrophilic moieties. Therefore, aqueous solutions of alcohols represent a rich test-ground for investigating hydration using theoretical approaches.

Generally, computer simulations of biomolecular systems are calculated using simple potential functions that do not account for many-body induced polarization effects explicitly. Induced polarization is typically incorporated in an average effective way. For example, widely used potential functions such as AMBER/parm94,<sup>16</sup> CHARMM27,<sup>29</sup> GROMOS,<sup>17</sup> and OPLS<sup>18</sup> are based on pairwise additive electrostatic interactions with fixed effective atomic partial charges that have been adjusted to account for the average induction arising in a typical environment. While such potential functions can be remarkably successful in modeling complex molecular systems (e.g., see ref 19), a meaningful representation of the balance of hydration forces around polar and nonpolar moieties requires a careful consideration of induced polarization.<sup>21,22</sup> A polarizable model can produce a polarization response varying gradually with the composition of the mixture.

At the present time, computational chemists and biophysicists are actively pursuing the development of a new generation of force fields for biomolecular simulations.<sup>23–27</sup> Recently, a simple polarizable potential function for water molecule based on the classical Drude oscillator has been developed and implemented.<sup>28</sup> The current efforts are made within the framework of the CHARMM/PARAM-22 force field,<sup>29</sup> with the long-term goal of developing a complete polarizable potential function

<sup>†</sup> Part of the special issue “David Chandler Festschrift”.

<sup>\*</sup> Corresponding author e-mail: benoit.roux@med.cornell.edu.

<sup>‡</sup> Weill Medical College of Cornell University.

<sup>§</sup> On leave from the Institute of Solution Chemistry, Russian Academy of Sciences, Akademicheskaya Str. 1, Ivanovo, Russia, 153045.

<sup>||</sup> Université de Montréal.

for biomolecular simulations. A logical next step after water is to parametrize more complicated systems such as monatomic alcohols.<sup>24,25</sup> In addition to its obvious methodological interest, an accurate model of ethanol is very important to address a number of fundamental questions about the role of atomic polarizability regarding hydration phenomena.

The aims of the present paper are 2-fold. From a methodological perspective, we want to develop a new simple polarizable model for ethanol consistent with the existing CHARMM/PARAM-22 force field.<sup>28,29</sup> To ensure the validity of the model both in the gas- and condensed-phases, we parametrize it against a wealth of experimental information, complemented by quantum-chemical data on the ethanol gas-phase dipole moment, polarizability, and multiple dimer structures. At a more fundamental level, our goal is to elucidate the structure and dynamics underlying their abnormal mixing properties and to ascertain the significance of hydrophobic hydration in ethanol–water solutions for a wide range of concentration.

## Models and Methods

The intermolecular potential for the polarizable ethanol model is similar to the functional form used previously for the SWM4-DP water model.<sup>28</sup> Each atom is described by a partial point-charge  $q$  and a set of Lennard-Jones parameters  $\epsilon$  and  $\sigma$  (combined with the others following the usual Lorentz–Berthelot rules<sup>30</sup>). In addition, the heavy atoms carry an auxiliary Drude particle,<sup>28</sup> tethered by a harmonic spring with force constant  $k_D$ .

In a field  $\mathbf{E}$ , a Drude particle carrying a charge  $\delta q$  shifts its equilibrium, zero-field position, by  $d = \delta q \mathbf{E} / k_D$ , giving rise to an induced dipole  $\mu = \delta q^2 \mathbf{E} / k_D$ . Hence, the atomic polarizability created by a Drude model is  $\alpha = \delta q^2 / k_D$  and, assuming a uniform  $k_D = 1000$  kcal/mol/Å<sup>2</sup> for all three heavy atoms of the ethanol molecule, the charges  $\delta q$  can be adjusted to produce appropriate  $\alpha$  values. Within a given molecule, the induced atomic dipoles are coupled with a screened electrostatic interaction. The original scheme of Thole<sup>31</sup> was adapted to the present case where finite dipoles are formed of two point charges. For two interacting dipoles 1 and 2, the pair of charges  $\delta q_1$  and  $-\delta q_1$  interacts with the pair of charges  $\delta q_2$  and  $-\delta q_2$  via a screened Coulomb interaction. The interaction energy is the sum of four terms of the form:

$$\frac{\delta q_1 \delta q_2}{r_{12}} \left[ 1 - \left( 1 - \frac{\bar{r}_{12}}{2} \right) \exp(-\bar{r}_{12}) \right] \quad (1)$$

The normalized distance  $\bar{r}_{12}$  is defined as

$$\bar{r}_{12} = a \frac{r_{12}}{\sqrt[6]{\alpha_1 \alpha_2}} \quad (2)$$

where  $a$  is a dimensionless number that is adjusted empirically. This interaction creates a cooperativity among the induced dipoles that favors a longitudinal polarization in accord with ab initio calculations. The molecular polarizability of ethanol would be isotropic in the absence of this intramolecular coupling.

The parameter  $a$  is set to 2.6, a value that is known to create a correct polarizability anisotropy ratio for an idealized benzene molecule and that is similar to the various estimates of Thole<sup>31</sup> and van Duijnen and Swart.<sup>32</sup> Apart from the Thole dipole–dipole intramolecular interactions, we keep the original CHARMM/PARAM-22 intramolecular interactions<sup>29</sup> (bond stretch, angle bend, and torsion). The atomic charges and atomic

**TABLE 1: Parameters of the Polarizable Ethanol Model<sup>a</sup>**

| atom            | $q$ (e)   | $\alpha$ (Å <sup>3</sup> ) | $\epsilon$ (kcal/mol) | $\sigma$ (Å)    |
|-----------------|-----------|----------------------------|-----------------------|-----------------|
| O <sub>E</sub>  | −0.520351 | 0.977723                   | −0.1521               | 1.532345        |
| HO <sub>E</sub> | 0.361419  |                            | −0.046                | <i>0.200007</i> |
| C <sub>1</sub>  | 0.020246  | 1.217571                   | −0.055                | <i>1.937705</i> |
| H <sub>1</sub>  | 0.073583  |                            | −0.022                | <i>1.175986</i> |
| C <sub>2</sub>  | −0.269975 | 1.237576                   | −0.08                 | <i>1.835251</i> |
| H <sub>2</sub>  | 0.087165  |                            | −0.022                | <i>1.175986</i> |

<sup>a</sup> C<sub>1</sub> is the carbon atom bound to the oxygen, and C<sub>2</sub> is the carbon atom of the methyl group. H<sub>1</sub> is the two atoms of the C<sub>1</sub> group, and H<sub>2</sub> is the three atoms of the C<sub>2</sub> group. The parameters unchanged from the CHARMM/PARAM-22 force field are in italics.

polarizabilities (as well as the Lennard-Jones parameters for the ethanol oxygen) were adjusted to reproduce the essential properties of liquid ethanol: evaporation enthalpy, density, dielectric constant, and self-diffusion constant. All the parameters of the ethanol model are listed in Table 1. The oxygen atom is labeled O<sub>E</sub>, the carbon atom bound to the oxygen is labeled C<sub>1</sub>, and the final carbon is labeled C<sub>2</sub>. The other parameters are kept the same as in the CHARMM/PARAM-22 force field.<sup>29</sup> The proposed ethanol model reproduces fairly well the experimental value of the gas-phase dipole,  $\mu = 1.71$  D.<sup>33</sup>

The evaporation enthalpy ( $\Delta h$ ) is obtained from the average potential energy per molecule ( $\langle u \rangle_{\text{liq}}$ ) in the liquid phase relative to the average potential energy of a single molecule in the gas phase ( $\langle u \rangle_{\text{gas}}$ ). The latter is obtained from a Langevin dynamics simulation with the three induced dipoles kept in their energy minimum at every time of the simulation:

$$\Delta h = k_B T - (\langle u \rangle_{\text{liq}} - \langle u \rangle_{\text{gas}}) \quad (3)$$

The density is reported in terms of the molecular volume  $v = \langle V \rangle / N$ , where  $N$  is the number of molecules and  $\langle V \rangle$  is the average volume of the simulation box. The dielectric constant is computed from the fluctuations of  $\mathbf{M}$ , the total dipole moment of the box:<sup>34,35</sup>

$$\epsilon = \epsilon_\infty + \frac{4\pi}{3\langle V \rangle k_B T} (\langle \mathbf{M}^2 \rangle - \langle \mathbf{M} \rangle^2) \quad (4)$$

The high-frequency contribution ( $\epsilon_\infty$ ), which is not produced by inducible dipoles in the self-consistent field regime, is estimated from the Clausius–Mossotti equation:<sup>36</sup>

$$\frac{\epsilon_\infty - 1}{\epsilon_\infty + 1} = \frac{4\pi}{3} \frac{\alpha}{v} \quad (5)$$

For the present ethanol model at its equilibrium density,  $\epsilon_\infty = 1.69$ . The self-diffusion constant ( $D$ ) is computed from the mean-squared displacement of the oxygen atoms. For the MD simulations of the mixtures, this ethanol model is combined with the SWM4-DP water model of Lamoureux et al.<sup>28</sup> The water oxygens will be referred to as O<sub>w</sub>. All MD simulations are performed in the NPT ensemble at room temperature and pressure ( $T = 300$  K and  $P = 1$  atm) using a double-thermostat scheme described previously.<sup>28</sup> The dipoles are maintained in the self-consistent-field induction regime using an additional low-temperature thermostat.<sup>37</sup> The integration time step is 2 fs. Cubic periodic boundary conditions with particle-mesh Ewald summation algorithm<sup>38</sup> were used to treat long-range electrostatic interactions. Truncation of van der Waals interactions is accounted for by an effective long-range correction.<sup>39</sup> The primary cubic box contains 250 molecules for all simulations. The initial dimensions of the box were set up according to the experimental density of ethanol and ethanol–water solutions.<sup>33</sup>

TABLE 2: Computed and Experimental Properties for Ethanol

|  | this work      | PARAM-22 <sup>29</sup> | OPLS <sup>41,42</sup> | PIPF <sup>25</sup> | ab initio/expt               |
|--|----------------|------------------------|-----------------------|--------------------|------------------------------|
| <i>trans</i> – <i>trans</i> Ethanol Dimer  |                |                        |                       |                    |                              |
| $E_{\text{int}}$ (kcal/mol)                | −7.29          | −7.77                  | −7.04                 | −6.19              | −4.86 to −7.96 <sup>40</sup> |
| $r_{\text{O} \cdots \text{O}}$ (Å)         | 2.79           | 2.80                   | 2.74                  | 2.74               | 2.84 <sup>40</sup>           |
| <i>gauche</i> – <i>trans</i> Ethanol Dimer |                |                        |                       |                    |                              |
| $E_{\text{int}}$ (kcal/mol)                | −7.79          | −7.78                  |                       |                    | −4.82 to −8.16 <sup>40</sup> |
| $r_{\text{O} \cdots \text{O}}$ (Å)         | 2.79           | 2.81                   |                       |                    | 2.86 <sup>40</sup>           |
| Liquid-State Properties                    |                |                        |                       |                    |                              |
| $\Delta h$ (kcal/mol)                      | 10.19          | 9.68                   | 10.23                 | 10.09              | 10.15 <sup>74</sup>          |
| $\epsilon$                                 | $24.1 \pm 1.2$ | $17.1 \pm 0.6$         | $16.1 \pm 0.4$        | $23.9 \pm 0.4$     | 24.3 <sup>48</sup>           |
| $D$ ( $10^{-5}$ cm <sup>2</sup> /s)        | 0.967          | 1.59                   | 1.56                  | 1.09 <sup>75</sup> |                              |

All ethanol–water mixtures were simulated for 3 ns. To get a better convergence, the pure ethanol system was simulated for 6 ns.

## Results and Discussion

**Gas-Phase Properties.** The first step in validating the ethanol model is to examine its ability to accurately reproduce the geometries and energies of various hydrogen-bonded complexes from previous studies. Table 2 summarizes the results for the present polarizable model along with available quantum-chemical computations<sup>40</sup> and molecular-mechanical computations using the CHARMM/PARAM-22 force field,<sup>29</sup> the OPLS force field,<sup>41,42</sup> and the polarizable PIPF force field of Gao et al.<sup>25</sup> It should be noted that results from the current model are similar to previous studies using OPLS potential<sup>41</sup> and quantum chemistry computations.<sup>40</sup> The oxygen–oxygen distance is very similar to those of the OPLS potential model, which is about 0.1 Å shorter than the same distance from ab initio estimates.

**Liquid Ethanol.** The simulated and experimental results on enthalpy of evaporation are presented in Table 2 for different potential models. The performance of all models are comparable and agree well with experimental results. The computed molecular volume differs from experiment by only 2.7%, which is comparable or better than results from previous simulations.<sup>25,41,42</sup> Compared to nonpolarizable models,<sup>42,43</sup> the inclusion of polarizability is expected to improve the accuracy of the model for simulating self-diffusion coefficient and dielectric constant. The change in molecular dipole moment of ethanol transferring from the gas phase to the liquid is a good indicator of the condensed-phase polarization effect. The average dipole in neat liquid ethanol is 2.38 D compared to 1.71 D in the gas phase. Although it is lower than experimental<sup>44</sup> or Car–Parrinello (CP) molecular dynamics<sup>45</sup> estimates (3.04 and 3.1 D, respectively), this value is needed to correctly reproduce the dielectric constant of the liquid.

The structure of the liquid can be characterized by a number of pair-distribution functions (RDFs). Figure 1 summarizes two of the most important RDFs for ethanol together with the running integration numbers. There is a displacement of the first peak in the  $\text{O}_\text{E} \cdots \text{O}_\text{E}$  and  $\text{O}_\text{E} \cdots \text{H}_\text{E}$  RDFs in comparison to nonpolarizable models.<sup>41</sup> Experimental results indicate a first peak in the  $\text{O}_\text{E} \cdots \text{O}_\text{E}$  RDFs at around 2.7–2.8 Å, with a coordination number of 1.8–2.0.<sup>46,47</sup> These observations are in reasonable agreement with the present results, which yield a coordination number of 1.94 (by integration of the  $\text{O}_\text{E} \cdots \text{O}_\text{E}$  RDFs to the minimum at 3.45 Å). Hydrogen-bonding interactions in ethanol are reflected in the strong first peak in the  $\text{O}_\text{E} \cdots \text{H}_\text{E}$  distribution function (Figure 1). The first maximum is around 1.75 Å for the polarizable model and 1.85 Å for the CHARMM/PARAM-22 force field. The integration of each distribution function to the position of the first minimum gives coordination number of 0.96 (up to 2.55 Å) and 0.95 (up to 2.60 Å) for

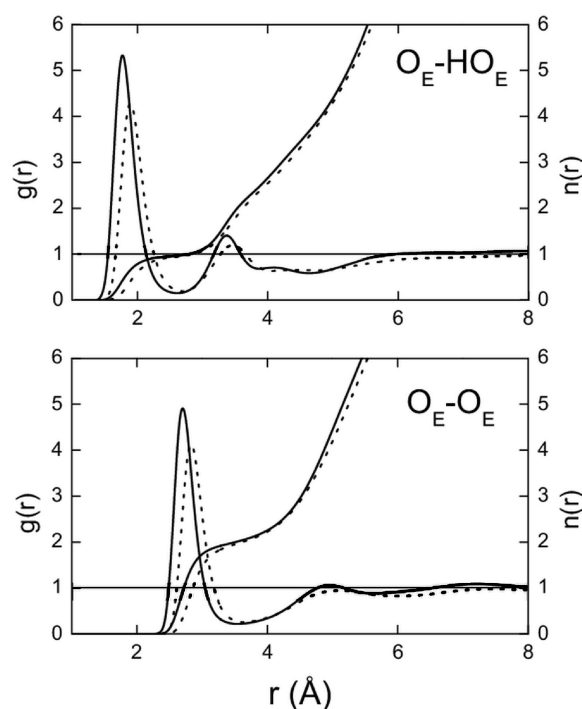
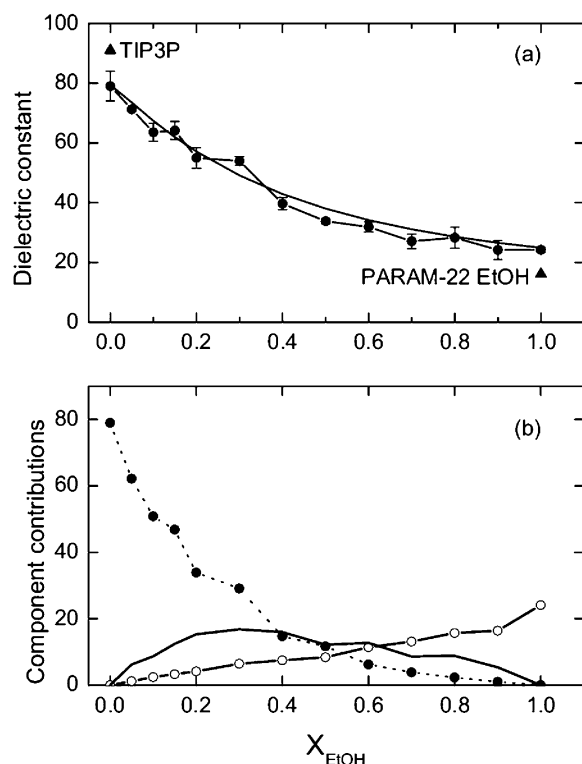


Figure 1.  $\text{O}_\text{E} \cdots \text{HO}_\text{E}$  and  $\text{O}_\text{E} \cdots \text{O}_\text{E}$  radial distribution functions with running integration numbers (solid line: this work; dotted line: CHARMM/PARAM-22 force field).

polarizable and nonpolarizable potential models, respectively. It was found that the use of a long-range correction<sup>39</sup> to the summation of the van der Waals dispersion terms is essential for a precise simulation of the volume in NPT simulations. Similar conclusions were reached for liquid alkanes.<sup>39</sup>

**Water–Ethanol Mixtures.** The  $\text{O}_\text{E} \cdots \text{O}_\text{w}$ ,  $\text{C}_1 \cdots \text{O}_\text{w}$ , and  $\text{C}_2 \cdots \text{O}_\text{w}$  RDFs were computed for all concentrations (see the Supporting Information). For diluted ethanol mixtures, the water structure around ethanol is similar to the results at infinite dilution of Fidler and Rodger<sup>11</sup> and van Erp and Meijer.<sup>45</sup> The positions and shapes of all peaks are comparable, though the  $\text{O}_\text{E} \cdots \text{O}_\text{w}$  peak is higher in the current simulations.

**Dielectric Properties.** A demanding test for the transferability of the polarizable force field is the accurate reproduction of the dielectric behavior of binary mixtures as a function of molar fractions of water and ethanol. The dependence of the dielectric constant on the mixture compositions, estimated from the MD simulations, is depicted in Figure 2 along with experimental data.<sup>48</sup> The inclusion of explicit polarizability succeeds in reproducing the variation of the static dielectric constant accurately over the full molar fraction range. In contrast, nonpolarizable models for ethanol fail to reproduce  $\epsilon$ . Perhaps additional parametrization is required to the correct description of the dielectric constants by simulations with nonpolarizable



**Figure 2.** (a) Dependence of the dielectric constant on the composition of the ethanol–water mixtures (circles: this work; solid line: experiment at 20 °C<sup>48</sup>). Results for pure TIP3P liquid<sup>48,49</sup> and pure CHARMM/PARAM-22 ethanol (triangles) are shown for comparison. The results for pure SWM4-DP liquid are from ref 28. (b) Contribution of the water component (full symbols), the ethanol component (empty symbols), and water–ethanol dipole cross-correlations (solid line, no symbols) to the dielectric constant of panel a.

models for ethanol. The uncertainty on the dielectric constant estimates from MD simulations, especially in the 0.50–0.80 range of ethanol molar fraction, is due to the slow convergence in fluctuations of the total dipole.

Figure 2b shows the contributions to  $\epsilon$  of the water and ethanol components of the mixture. The expression  $\langle \mathbf{M}^2 \rangle - \langle \mathbf{M} \rangle^2$  of eq 4 is expanded into contributions from the fluctuations of the total dipole created by the water molecules,  $\langle \mathbf{M}_w^2 \rangle - \langle \mathbf{M}_w \rangle^2$ ; from the fluctuations of the dipole created by the ethanol molecules,  $\langle \mathbf{M}_{\text{EtOH}}^2 \rangle - \langle \mathbf{M}_{\text{EtOH}} \rangle^2$ ; and from the correlated fluctuations for both components,  $2\langle \mathbf{M}_w \cdot \mathbf{M}_{\text{EtOH}} \rangle - \langle \mathbf{M}_w \rangle \cdot \langle \mathbf{M}_{\text{EtOH}} \rangle$ . Interestingly, it reveals that dipole fluctuation cross-correlations are maximum in the  $X_{\text{EtOH}} = 0.2$ –0.4 range. Those might be related to the presence of a cooperative dynamics between water and ethanol in this range of concentrations.

Upon dilution in water, the average dipole of the ethanol molecule changes smoothly from 2.38 D in pure liquid ethanol to about 2.75 D at infinite dilution in liquid water. By comparison, the average molecular dipole of water goes from 2.45 D in pure water to approximately 2.37 D in pure ethanol (see Supporting Information, Figure S3). These variations signals the importance the polarity of the surrounding medium on the molecules. Over the whole range of ethanol–water mixtures, the magnitude of the dipole of ethanol changes by 0.37 D. These changes, which affect all ethanol–ethanol as well as ethanol–water intermolecular interactions, make it necessary to account for the induced polarization explicitly in such system. The contribution of each polarizable atom to the total induced dipole varies with ethanol concentration. Surprisingly, the  $C_1$  and  $C_2$  atoms are contributing almost half the total induced dipole per

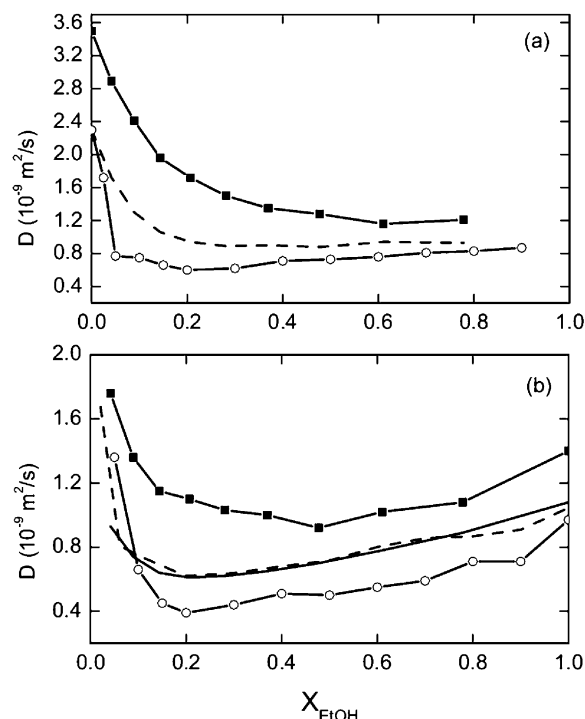


**Figure 3.** Self-diffusion coefficients for (a) water and (b) ethanol as function of molar fraction of ethanol. The empty circles are the results for the present work. Available experimental (solid<sup>76</sup> and dashed<sup>77</sup> lines, no symbols) and theoretical<sup>50</sup> (nonpolarizable OPLS force field, square symbols) data are depicted for both species.

molecule (see Supporting Information). For pure ethanol, the apolar part of the molecule has an induced dipole of 0.35 D, in agreement with the CP simulations of van Erp and Meijer.<sup>45</sup> At a molar fraction of  $X_{\text{EtOH}} = 0.05$ , it contributes as much as the polar oxygen (see Supporting Information).

**Dynamics.** Many of the anomalous properties of alcohol–water mixtures result from inhomogeneous mixing at different compositions. One of the salient characteristics of the nonideality in ethanol–water mixtures is the variation of the self-diffusion coefficients as a function of molar fraction of alcohol. Computed and experimentally measured self-diffusion coefficients for water and ethanol are depicted in Figure 3. Remarkably, the present model is able to reproduce the position of the minima in the self-diffusion coefficients for water ( $X_{\text{EtOH}} = 0.3$ ) and ethanol ( $X_{\text{EtOH}} = 0.2$ ). In contrast, MD studies of ethanol–water mixtures using nonpolarizable OPLS model for ethanol and TIP4P for water<sup>50</sup> do not reproduce this important feature of the ethanol–water mixtures.

A number of possible explanations of the nonlinear dependence of diffusion characteristics have been proposed over the past decade.<sup>76,77</sup> It was hypothesized that the large drop in the self-diffusion coefficients of water with a small increase of ethanol concentration ( $X_{\text{EtOH}} \approx 0.05$ –0.10) was caused by the existence of clathrate-like hydrates. Nuclear magnetic resonance studies<sup>51</sup> and molar excess enthalpy measurements<sup>52</sup> generally support the idea that the hydrogen bond network between water molecules surrounding the alkyl group is strengthened. However, diffraction studies do not substantiate this view in dilute water–alcohol mixtures.<sup>9,53</sup> The minimum of ethanol self-diffusion around  $X_{\text{EtOH}} \approx 0.2$  was associated with competitive self-association of ethanol and water by measurements of the dielectric relaxation and permittivity spectra.<sup>54</sup> Compressibility measurements<sup>55</sup> suggested that the hydrophobic hydration becomes negligible after  $X_{\text{EtOH}} \approx 0.3$  (minimum in water self-



diffusion). It was hypothesized that water starts to mix with ethanol as a single molecule after  $X_{\text{EtOH}} \approx 0.3$  (minimum in water self-diffusion). Contrary to these results, recent structural studies of methanol–water solutions suggested that water still forms hydrogen-bonded clusters, even at a very high alcohol concentrations.<sup>20</sup> Despite the numerous experiments, these questions are not resolved. It may be hoped that the current MD simulations offer a realistic and accurate description of the microscopic properties of ethanol–water mixtures. This provides a unique opportunity to address some of the questions about local structure effect and its influence on dynamics in water–ethanol mixtures.

**Hydrogen-Bonding Analysis.** Radial pair distribution functions, despite their usefulness, do not reveal all the complex structural aspects of the mixtures. To complement the RDF analysis, we analyzed the three-dimensional topology and clustering of the solute and solvent molecules as a function of ethanol concentration.

For the present analysis, two molecules are considered to be H-bonded if their  $\text{H}\cdots\text{O}$  distance is less than 2.4 Å and if the  $\text{O}-\text{H}\cdots\text{O}$  angle is larger than 150°. This definition is similar to that of Ferrario et al.,<sup>56</sup> of De Loof et al.,<sup>57</sup> and of Luzar and Chandler.<sup>58,59</sup> An energetic definition of the H-bond is not practical, as the energy of the polarizable model is not pairwise decomposable. For each MD configuration, the list of donor–acceptor pairs matching the H-bond definition is compiled into a set of H-bonding statistics. Because there is no perfectly objective definition of a H-bond, the H-bond counts should be compared to the analogous count for a reference liquid (pure water or pure ethanol).

#### Average Hydrogen-Bonding in Water–Ethanol Mixtures.

For pure liquid water, we find an average of 3.03 H-bonds per water molecule with the  $(d_{\text{HO}} < 2.4 \text{ Å})/150^\circ$  geometric definition of the H-bond. This value is smaller than the coordination number of 4.63 for neighboring oxygens,<sup>28</sup> reflecting the weakening/breakage of hydrogen bonds in tetrahedrally arranged water molecules throughout the simulation. The 3.03 value is consistent with other studies. From simulations calibrated against neutron diffraction data and a  $(d_{\text{OO}} < 3.5 \text{ Å})/150^\circ$  definition, Soper et al.<sup>60</sup> obtained 3.58 H-bonds per molecule. From an MD simulation of pure water using the TIP4P potential<sup>49</sup> and a  $(d_{\text{OO}} < 3.5 \text{ Å})/(U_{\text{int}} < -2.6 \text{ kcal/mol})$  definition of the H-bond, Oleinikova et al.<sup>61</sup> obtained 3.26 H-bonds per molecule. The contrasting X-ray absorption and X-ray Raman scattering measurements of Wernet et al.,<sup>62</sup> yielding  $2.2 \pm 0.5$  H-bonds per molecule, suggest the picture of a hydrated water molecule forming two strong and two weak H-bonds. Recent ab initio molecular simulations by Kuo and Mundy<sup>63</sup> yield 2.5 H-bonds per molecule in the bulk phase but only 1.9 H-bonds for molecules near a liquid–vapor interface [using a  $(d_{\text{OH}} < 2.27 \text{ Å})/140^\circ$  definition]. From our simulation of pure liquid ethanol, we find 1.65 H-bonds per molecule; the  $\text{O}_\text{E}-\text{O}_\text{E}$  coordination number is 1.94. Overall, these comparisons indicate that the coordination number of the oxygen–oxygen RDF is a somewhat biased estimator of the number of H-bonds.

Figure 4 shows the average total number of H-bonds per molecule as the ethanol concentration is increased. This total number includes contributions from both water and ethanol molecules. The top graph is showing the number of H-bonds per water molecule, broken down into contributions from water–water (W/W) and water–ethanol (W/E) H-bonds. The bottom graph is showing the same analysis for the ethanol component of the mixtures (ethanol–ethanol (E/E) and ethanol–water (E/W)). The deviations of these curves from ideal straight

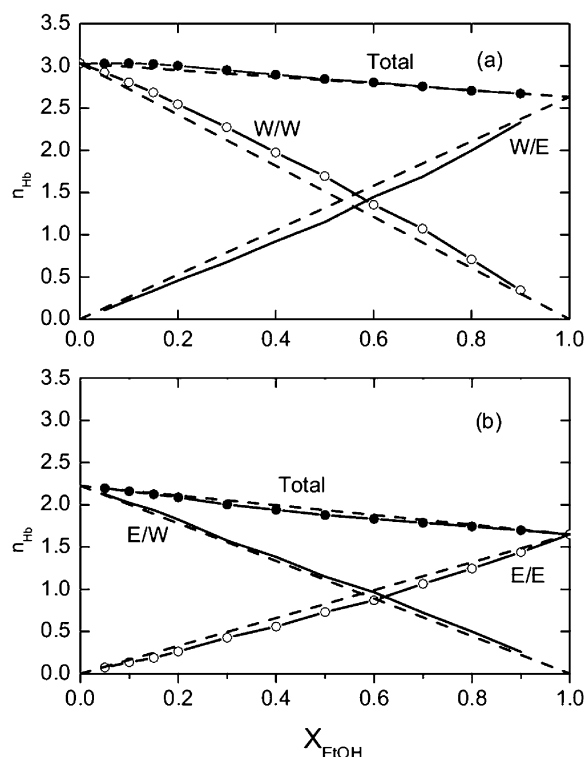


**Figure 4.** Average number of hydrogen bonds per molecule ( $n_{\text{Hb}}$ ) for (a) water and (b) ethanol. In panel a, the total  $n_{\text{Hb}}$  per water molecule is broken down into water–water (W/W) and water–ethanol (W/E) contributions. In panel b, the total per ethanol molecule is broken down into ethanol–water (E/W) and ethanol–ethanol (E/E) contributions. The straight dotted lines represent the ideal mixing.

lines correspond to the excess H-bonding. The positive excesses for the W/W and E/W curves and the negative excesses for the W/E and E/E curves are indicating that water is an overall better solvent than ethanol: at any ethanol fraction, both water and ethanol are preferably solvated by water.

At high-ethanol concentrations, the number of H-bonds decreases to 2.64 per water molecule. In other words, a water molecule solvated in pure ethanol loses only 14% of its H-bonding relative to pure liquid water. In comparison, the solvation of ethanol is enhanced by its dilution in water, going from 1.65 to 2.23 H-bonds per ethanol as  $X_{\text{EtOH}}$  goes from 1 to 0. For  $X_{\text{EtOH}}$  larger than 0.50, the excess of water–water H-bonds per water molecule is almost exactly compensated by the deficit of ethanol–water H-bonds per water molecule. This compensatory effect makes the total H-bonding per water appear like it is following the ideal mixing curve. For  $X_{\text{EtOH}}$  less than 0.50 however, there is a positive excess in the total H-bonding of water (see Figure 4a). Such an increase is the usual signature of the hydrophobic hydration.<sup>55,64</sup> The increase is sufficiently large that the total number of H-bonds for water molecules is actually stronger at low-ethanol concentrations than in pure water. The number of H-bonds per water molecule is maximum around  $X_{\text{EtOH}} = 0.10$ . Knowing that the water–water H-bonding dominates the thermodynamics at low ethanol concentration, this could be related to the maximum in excess enthalpy and entropy at  $X_{\text{EtOH}} \approx 0.10$  and a maximum in excess free energy at  $X_{\text{EtOH}} = 0.18\text{--}0.22$  observed from dielectric relaxation measurements.<sup>5,7,65,66</sup> What is not clear, however, is the nature of these H-bond-rich regions and how they are affected by the increase in ethanol concentration.

**Structure of Hydrogen-Bonding around Ethanol.** Figure 5a,b shows two isosurfaces for the density of water oxygen

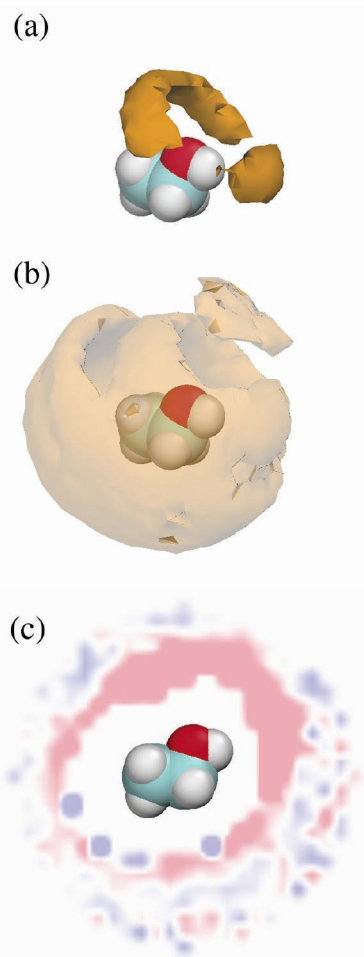


**Figure 5.** Water oxygen density around the closest ethanol molecule for  $X_{\text{EtOH}} = 0.05$ . Two isosurface are shown: the higher-density surface of panel a illustrates the first hydration shell of the ethanol hydroxyl group, and the lower-density surface of panel b shows the overall packing of water around the hydrophobic group and the second hydration shell of the ethanol hydroxyl. (c) Hydrogen bonding excess for a water molecule at a given position with respect to the closest ethanol molecule. Blue denotes regions where the water molecule forms more H-bonds than the bulk average, and red denotes regions where it forms less H-bonds than the bulk average. This function is presented for a slice in the  $\text{O}_\text{E}-\text{C}_1-\text{C}_2$  plane of the ethanol molecule and up to a distance of 6 Å from the  $\text{C}_1$  atom (after which the average value gets noisier because of a lack of sampling).

around ethanol at  $X_{\text{EtOH}} = 0.05$  (the lowest ethanol concentration simulated). The highest-density surface (Figure 5a, in opaque yellow) shows the first coordination shell of the ethanol hydroxyl group (in the trans conformation). It is divided into a relatively confined region where one water molecule is an acceptor to the ethanol hydroxyl and a wide band in which water acts as a proton donor. The lower-density surface (Figure 5b, in translucent yellow)—still higher than the bulk density—shows an accumulation of water at the surface of the hydrophobic group as well as a water-rich “cap” region where water can coordinate first-hydration-shell water molecules in both lobes of Figure 5a. The strong water–ethanol H-bonds are giving rise to a visible secondary density maximum on two sides of the ring-shaped isosurface of Figure 5a.

To complement this structural information, we examine the average number of H-bonds a water molecule at a position  $\mathbf{r}$  relative to the closest ethanol will form with any other molecule (water or ethanol, including the reference ethanol molecule). Figure 5c shows the distribution  $n_{\text{Hb}}(\mathbf{r})$  for a slice in the  $\text{O}_\text{E}-$

$\text{C}_1-\text{C}_2$  plane of the reference ethanol molecule. Because  $n_{\text{Hb}}$  is the number of hydrogen bonds per molecule, its value at a point  $\mathbf{r}$  is not directly related to the probability of a water molecule actually being there.

The regions where a water molecule makes less H-bonds than the bulk average (in red in Figure 5c) are where it is the most strongly bonded to ethanol (i.e., in the first hydration shell of the ethanol hydroxyl and, to a lesser extent, anywhere within H-bonding distance). In contrast, the water molecules in a narrow region of the first coordination shell of the nonpolar group have a H-bonding above the bulk average. This seems to conjure up the classical “clathrate” or “iceberg” picture of the hydrophobic hydration,<sup>4</sup> but overall, the net contribution to the excess water H-bonding from the first coordination shell of the nonpolar and hydroxyl groups is negative.

The average positive H-bonding excess reported in Figure 4 is in fact explained by the secondary hydration structure of ethanol. There is a small but significant H-bonding excess in most of the second shell (see Figure 5c). Although it is small, it involves a larger number of water molecules and creates a positive net contribution to the water H-bonding excess that compensates for the negative contribution from the first hydration shell.

This can be quantified by integrating the contributions to the excess number of water H-bonds from concentric shells centered around the closest  $\text{C}_1$  atom:

$$N_{\text{Hb}}^{(\text{xs})}(R) = \int_0^R dr [\rho_{\text{Hb}}(r) - n_{\text{Hb}}^{(\text{id})} \rho_{\text{O}}(r)] \quad (6)$$

$\rho_{\text{Hb}}(r)$  is the total number of H-bonds for the water molecules whose oxygen atom is in the shell of radius  $r$  and thickness  $dr$ , and  $\rho_{\text{O}}(r)$  is the number of such oxygen atoms. The ratio of local densities  $\rho_{\text{Hb}}(r)/\rho_{\text{O}}(r)$  corresponds to  $n_{\text{Hb}}(r)$ , the average number of H-bonds for a single water molecule in the shell of radius  $r$ . It is the radial average of the quantity presented in the contour plot of Figure 5c. The value  $n_{\text{Hb}}^{(\text{id})}$  is the number of H-bonds expected from an ideal, noninteracting water–ethanol mixture:

$$n_{\text{Hb}}^{(\text{id})} = 3.03 - X_{\text{EtOH}} \times (3.03 - 2.64) \quad (7)$$

This number depends on the concentration, and can be read from the dashed line under the total curve of Figure 4a. The excess H-bonding  $n_{\text{Hb}}(r)$  (corresponding to the quantities inside the square brackets of eq 6, divided by  $\rho$ ) and the running integrals  $N_{\text{Hb}}^{(\text{xs})}(R)$  are presented in Figure 6 for the low ethanol concentrations. They all converge to positive values, reflecting the fact that the water H-bonding is always in excess. Consistent with Figure 4a, the maximum water H-bonding excess is for  $X_{\text{EtOH}} = 0.15$ . For  $X_{\text{EtOH}} = 0.05$ , an excess of H-bonding can be observed as far as 8 Å from the closest ethanol.

In Figure 6, the two vertical lines indicate the positions of the first maximum and first minimum in the  $\text{C}_1-\text{O}$  RDF. They are not changing significantly in this low-ethanol concentration range. This shows that, although some water molecules in the outer region of the first shell may have a positive excess H-bonding, they are not contributing sufficiently to compensate for the negative excess H-bonding in the first shell. This suggests that the excess H-bonding is not due to the water in the first hydration shell, where the classical “clathrate” structure would be found. The distance at which the positive excess H-bonding overcomes the negative excess can be read directly from the intersection of the integral (in dashed line) with the zero-abscissa horizontal line. It gets shorter as the ethanol concentration increases but, interestingly, does not quite penetrate the first

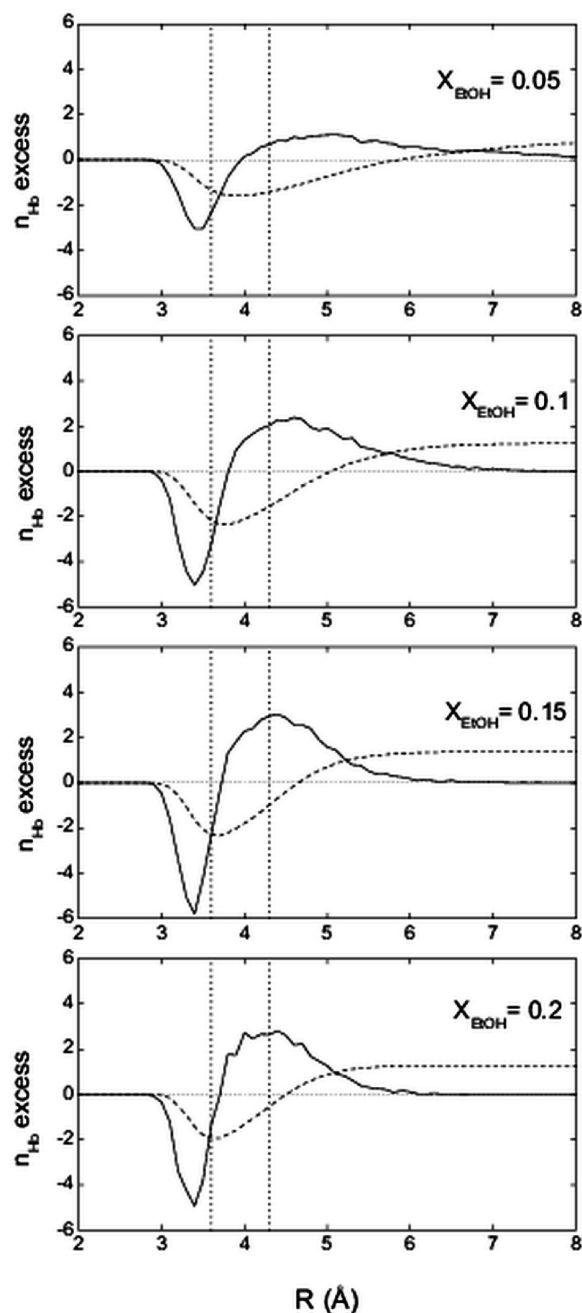


**Figure 6.** Radial distributions (solid lines) of the excess  $n_{Hb}$  for a water molecule at given distance from the nearest  $C_1$  atom. The dashed lines are the running integrals  $N(R)$  (see text) and represent the total H-bonding excess. The dashed vertical lines show the positions of the first peak of the  $C_1$ –O RDF and of the density minimum between the first and second solvation shells.

hydration shell. At  $X_{EtOH} = 0.20$ , a significant compensation is occurring in the first shell (around 4 Å), but the negative excess is still overcome in the second hydration shell (around 5–6 Å). A similar “compaction” of the first hydration shell was noticed by Dixit et al.,<sup>9</sup> who also suggested that it could be explaining the entropic contribution to the hydrophobic interaction.

The analysis of Figure 6 cannot be done for  $X_{EtOH} \geq 0.40$  because the ethanol molecules are too condensed for a secondary hydration structure to be significantly populated. Any water molecule in the second hydration shell of one ethanol molecule is also in the first shell of another. At such concentration, the excess integrals are close to zero, and never become significantly negative for higher ethanol fraction (as shown in Figure 4a).

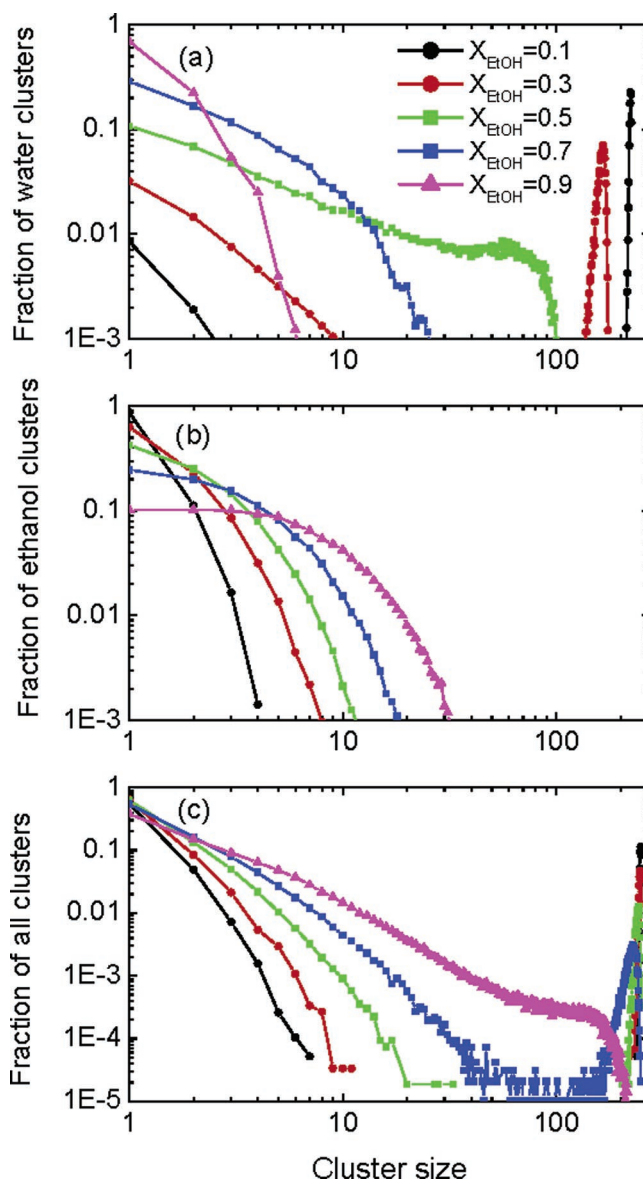


**Figure 7.** Molar contribution of H-bonded clusters in terms of their sizes for (a) pure-water clusters, (b) pure-ethanol clusters, and (c) mixed water–ethanol clusters. It is the molar contribution to the water component of the mixture for panel a, the ethanol component of the mixture for panel b, and the whole liquid for panel c.

This could be explained by the fact that the water clusters are robust enough to provide for themselves the contribution of the water–water H-bonding missing at high-ethanol concentration.

**Hydrogen-Bonded Clusters.** Liquid water is characterized by the existence of an extensive inter-connected network of hydrogen bonds that percolates throughout the entire phase.<sup>67,68</sup> Such a view is confirmed by the simulations based on the SWM4-DP model. Indeed, cluster analysis of the H-bond connectivity of pure water<sup>28</sup> reveals a H-bonding network extending over the whole liquid. It shows that less than 1% of the molecules are not connected to the bulk H-bond network. Upon the admixture of ethanol, the H-bond network of any type (water–water, water–ethanol, or ethanol–ethanol) becomes less dense, and larger disconnected clusters begin to be observed. Figure 7 presents the distribution of H-bonded cluster sizes (number of participating molecules).

According to Figure 7a, a sufficiently high concentration of ethanol breaks the percolating water network. For  $X_{EtOH} \leq 0.3$ , most of the water component is forming extensive clusters of



sizes close to the total number of water molecules in the simulation box. For  $X_{\text{EtOH}} = 0.7$ , most of the water is forming small clusters (significantly smaller than the total 75 water molecules in the simulation). The critical percolation point of the water network appears to be for  $X_{\text{EtOH}}$  slightly less than 0.5. At this concentration, cluster of all sizes can be observed, their distribution obeying approximately a power law.<sup>69</sup> From randomly generated liquid structures constrained by experimental data as well as from standard MD simulations, Dougan et al.<sup>70</sup> found a comparable critical fraction (near 0.54) for methanol–water mixtures. Our analysis is also consistent with the results of neutron-diffraction scattering, showing nonideal mixing of water at  $X_{\text{EtOH}} = 0.7$ .<sup>20</sup>

The cluster analysis shows that, at  $X_{\text{EtOH}} = 0.90$ , 69% of the water component is present as dispersed monomers, 22% as water dimers, 5% as water trimers, and 2% as water tetramers (see Figure 7a). At  $X_{\text{EtOH}} = 0.70$ , 29% of the water are monomers, 17% are dimers, 11% are trimers, and 9% are tetramers. This is consistent with the neutron-diffraction results of Dixit et al.<sup>20</sup> for methanol–water mixtures, which show that, at a methanol fraction of 0.7, only a small fraction of the water component is monomeric.

Because of its lower H-bonding capability, small clusters of 1–5 molecules disconnected from the bulk network contain mostly ethanol. At  $X_{\text{EtOH}} = 0.10$ , approximately 25% of all the single molecules not forming any H-bond are ethanol. Interestingly, this bias persists for clusters of mesoscopic sizes (at least at ethanol concentrations high enough for these clusters to be seen). For  $X_{\text{EtOH}} = 0.90$ , clusters up to 20 molecules contain on average more than 90% ethanol. For  $X_{\text{EtOH}} = 0.70$ , clusters up to 50 molecules contain on average more than 70% ethanol.

The most striking observation from Figure 7b is that the ethanol component of the mixture does not percolate at any concentration point. This suggests that the mechanism of proton mobility in ethanol could be qualitatively different from the Grotthuss mechanism proposed for pure water<sup>71</sup> and might involve a reorganization of the H-bonding structure as described by Morrone and Tuckerman<sup>72</sup> for pure methanol. Alternatively, if one considers the network formed of any type of H-bond (see Figure 7c), it appears that the presence of a relatively small amount of water ( $X_{\text{EtOH}} < 0.3$ ) forms a percolating two-component network from the ethanol clusters (which are by themselves nonpercolating, see Figure 7b). This may, perhaps, be related to the maximum observed in the ethanol–water cross-contribution to the dielectric constant around the same molar fraction, as the total dielectric constant depends on the fluctuations of the total dipole.<sup>35</sup> The formation of a two-component percolating network affects the H-bonding between water molecules and ethanol clusters at  $X_{\text{EtOH}} < 0.2$ . There is optimal number of water molecules to solvate each ethanol molecule at  $X_{\text{EtOH}} = 0.2$ . This provides an energetical and structural basis for the existence of the quasi-stable H-bonded ethanol–water clusters and suggests an explanation for the slow increase in the self-diffusion coefficients for  $X_{\text{EtOH}}$  larger than 0.2 (see Figure 3). For methanol–water solutions, Dougan et al.<sup>70</sup> observed that the self-diffusion coefficient reaches a minimum in the same concentration regime; they noted that this is the point where both the H-bonding network of water and the hydrophobic packing network of methanol are percolating. This mixed water–ethanol network is critically percolating at  $X_{\text{EtOH}}$  slightly less than 0.9. Although the exact point at which this percolation transition occurs cannot be determined very accurately because of the finite size of the simulation box (250

molecules) and the finite simulation time, its existence is unambiguous.

## Summary

A polarizable model for ethanol was parametrized to reproduce the vaporization enthalpy, static dielectric constant, and self-diffusion constant of the neat liquid at ambient conditions. It was used in combination with the polarizable SWM4-DP water model<sup>28</sup> to investigate the structural and dynamical origins of the phenomenon observed in water–ethanol mixtures. Even though the ethanol model was parametrized independently of the water model, the properties of the mixtures obtained from MD simulations are in excellent agreement with experiment. The dielectric constant is correctly reproduced across the whole ethanol concentration range (see Figure 2). The important features of the water and ethanol mobilities are reproduced as well: a rapid decrease in diffusivity for low ethanol concentration, an absolute mobility minimum at  $X_{\text{EtOH}} \sim 0.2$ , and a gradual increase as the ethanol concentration gets higher (see Figure 3). An important aspect of the polarizable model is that it produces a polarization response gradually with the composition of the mixture. That, of course, can be attained only with a model that accounts for induced polarization explicitly. It is not clear to what extent this feature explains the good accuracy obtained for the dielectric properties of the mixtures, but knowing how strongly the average induced dipole correlates with the dielectric constant,<sup>73</sup> it is undoubtedly a significant factor.

The present work suggests a unifying view on alcohol hydration. The current simulations support the notion that the water–water H-bonding is enhanced in the first hydration shell of the nonpolar group, as commonly assumed in the “iceberg” picture. But according to the simulations, such an effect does not dominate the overall structure because the water–water H-bonding is depleted in the neighborhood of the hydroxyl group. The net effect from the entire first hydration shell is a reduction rather than an excess of water H-bond, and the dominant contribution arises from the structuring of water in the second hydration shell of ethanol. The simulations also indicate the presence of water clustering at very high ethanol concentration and reveal the existence of a transition between a fully percolating network of H-bonded water molecules at low ethanol concentration to a nonpercolating H-bonded network at high ethanol concentration.

**Acknowledgment.** Useful discussions with C. L. Brooks III, M. G. Kiselev, A. D. MacKerell, and A. K. Soper are gratefully acknowledged. B.R. was supported by NIH Grant GM-072558 and by NSF Grant 0415784. S.Yu.N. was supported by the American Epilepsy Society and UCB Pharma Inc. Both S.Yu.N. and G.L. contributed equally to this work.

**Supporting Information Available:** Three figures showing oxygen–oxygen and carbon–oxygen functions for ethanol and molecular induction effects in ethanol and water. This material is available free of charge via the Internet at <http://pubs.acs.org>.

## References and Notes

- (1) Hummer, G.; Garde, S.; García, A. E.; Pratt, L. R. *Chem. Phys.* **2000**, 258, 349–370.
- (2) Huang, D. M.; Chandler, D. *Proc. Nat. Assoc. Sci.* **2000**, 97, 8324–8327.
- (3) Southall, N. T.; Dill, K. A.; Haymet, A. D. J. *J. Phys. Chem. B* **2002**, 106, 521–533.
- (4) Frank, H. S.; Evans, M. W. *J. Chem. Phys.* **1945**, 13, 507–532.



- (5) Boyne, J. A.; Williams, A. G. *J. Chem. Eng. Data* **1967**, *12*, 318–323.
- (6) Price, W. S.; Ide, H.; Arata, Y. *J. Phys. Chem. A* **2003**, *107*, 4784–4789.
- (7) Koga, Y.; Nishikawa, K.; Westh, P. *J. Phys. Chem. A* **2004**, *108*, 3873–3877.
- (8) Finney, J. L.; Bowron, D. T.; Soper, A. K. *J. Phys.: Condens. Matter* **2000**, *12*, A123–A128.
- (9) Dixit, S.; Soper, A. K.; Finney, J. L.; Crain, J. *Europhys. Lett.* **2002**, *59*, 377–383.
- (10) Finney, J. L.; Bowron, D. T.; Daniel, R. M.; Timmins, P. A.; Roberts, M. A. *Biophys. Chem.* **2003**, *105*, 391–409.
- (11) Fidler, J.; Rodger, P. M. *J. Phys. Chem. B* **1999**, *103*, 7695–7703.
- (12) Noskov, S. Y.; Kiselev, M. G.; Kolker, A. M.; Rode, B. M. *J. Mol. Liq.* **2001**, *91*, 157–165.
- (13) Kiselev, M.; Ivlev, D. *J. Mol. Liq.* **2004**, *110*, 193–199.
- (14) Dangelo, M.; Onori, G.; Santucci, A. *J. Chem. Phys.* **1994**, *100*, 3107–3113.
- (15) Egashira, K.; Nishi, N. *J. Phys. Chem. B* **1998**, *102*, 4054–4057.
- (16) Cornell, W. D.; Cieplak, P.; Bayly, C. I.; Gould, I. R.; Merz, K. M., Jr.; Ferguson, D. M.; Spellmeyer, D. C.; Fox, T.; Caldwell, J. W.; Kollman, P. A. *J. Am. Chem. Soc.* **1995**, *117*, 5179–5197.
- (17) van Gunsteren, W. F.; Daura, X.; Mark, A. E. The GROMOS force field. In *Encyclopedia of Computational Chemistry*; Wiley: Chichester, 1998; Vol. 2, pp 1211–1216.
- (18) Jorgensen, W. L.; Tirado-Rives, J. *J. Am. Chem. Soc.* **1988**, *110*, 1657–1666.
- (19) Karplus, M. *Acc. Chem. Res.* **2002**, *35*, 321–323.
- (20) Dixit, S.; Crain, J.; Poon, W. C. K.; Finney, J. L.; Soper, A. K. *Nature* **2002**, *416*, 829–832.
- (21) Dudev, T.; Lim, C. *Chem. Rev.* **2003**, *103*, 773–787.
- (22) Quiliin, M. L.; Breyer, W. A.; Griswold, I. J.; Matthews, B. W. *J. Mol. Biol.* **2000**, *302*, 955–977.
- (23) Kaminski, G. A.; Friesner, R. A.; Zhou, R. *J. Comput. Chem.* **2003**, *24*, 267–276.
- (24) Paolantoni, M.; Ladanyi, B. *J. Chem. Phys.* **2002**, *117*, 3856–3873.
- (25) Gao, J. L.; Habibollahzadeh, D.; Shao, L. *J. Phys. Chem.* **1995**, *99*, 16460–16467.
- (26) Patel, S.; Brooks, C. L., III. *J. Comput. Chem.* **2004**, *25*, 1–16.
- (27) Patel, S.; MacKerell, A. D.; Brooks, C. L., III. *J. Comput. Chem.* **2004**, *25*, 1504–1514.
- (28) Lamoureux, G.; MacKerell, A. D.; Roux, B. *J. Chem. Phys.* **2003**, *119*, 5185–5197.
- (29) MacKerell, A. D., Jr.; Bashford, D.; Bellot, M.; Dunbrack, R. L.; Evanseck, J. D.; Field, M. J.; Gao, J.; Guo, H.; Ha, S.; Joseph-McCarthy, D.; Kuchnir, L.; Kucsera, K.; Lau, F. T. K.; Mattos, C.; Michnick, S.; Nog, T.; Nguyen, D. T.; Prodhom, B.; Reiher, W. E.; Roux, B.; Schlenkrich, M.; Smith, J. C.; Stote, R.; Straub, J.; Watanabe, M.; Wiorkiewicz-Kuczera, J.; Karplus, M. *J. Phys. Chem. B* **1998**, *102*, 3586–3616.
- (30) Allen, M. P.; Tildesley, D. J. *Computer Simulation of Liquids*; Oxford University Press: Oxford, 1987.
- (31) Thole, B. T. *Chem. Phys.* **1981**, *59*, 341–345.
- (32) van Duijnen, P. T.; Swart, M. *J. Phys. Chem. A* **1998**, *102*, 2399–2407.
- (33) *International Critical Tables of Numerical Data, Physics, Chemistry and Technology*; Knovel: New York, 2003.
- (34) Kirkwood, J. G. *J. Chem. Phys.* **1939**, *7*, 911–919.
- (35) Neumann, M.; Steinhauser, O. *Chem. Phys. Lett.* **1984**, *106*, 563–567.
- (36) Buckingham, A. D. *Proc. R. Soc. London, Ser. A* **1956**, *238*, 235–244.
- (37) Lamoureux, G.; Roux, B. *J. Chem. Phys.* **2003**, *119*, 3025–3039.
- (38) Darden, T.; York, D.; Pedersen, L. *J. Chem. Phys.* **1993**, *98*, 10089–10092.
- (39) Lagüe, P.; Pastor, R. W.; Brooks, B. R. *J. Phys. Chem. B* **2004**, *108*, 363–368.
- (40) Provencal, R. A.; Casaes, R. N.; Roth, K.; Paul, J. B.; Chapo, C. N.; Saykally, R. J.; Tschumper, G. S.; Schaeffer, H. S., III. *J. Phys. Chem. A* **2000**, *107*, 1423–1429.
- (41) Jorgensen, W. L. *J. Phys. Chem.* **1986**, *90*, 1276–1284.
- (42) Saiz, L.; Padrò, J. A.; Guàrdia, E. *J. Phys. Chem. B* **1997**, *101*, 78–76.
- (43) Saiz, L.; Guàrdia, E.; Padrò, J. A. *J. Chem. Phys.* **2000**, *113*, 2814–2821.
- (44) McClellan, A. L. *Tables of Experimental Dipole Moments*; Rahara Enterprises: El Cerrito, CA, 1989.
- (45) van Erp, T. S.; Meijer, E. J. *J. Chem. Phys.* **2003**, *118*, 8831–8840.
- (46) Benmore, C. J.; Loh, Y. L. *J. Chem. Phys.* **2000**, *112*, 5877–5883.
- (47) Narten, A. H.; Habenschuss, A. *J. Chem. Phys.* **1984**, *80*, 3387–3391.
- (48) Åkerlöf, E. *J. Am. Chem. Soc.* **1932**, *54*, 4125–4139.
- (49) Jorgensen, W. L.; Chandrasekhar, J.; Madura, J. D.; Impey, R. W.; Klein, M. L. *J. Chem. Phys.* **1983**, *79*, 926–935.
- (50) Wensink, E. J. W.; Hoffmann, A. C.; van Maaren, P. J.; van der Spoel, D. *J. Chem. Phys.* **2003**, *119*, 7308–7317.
- (51) Mizuno, K.; Miyashita, Y.; Shindo, Y.; Ogawa, H. *J. Phys. Chem.* **1995**, *99*, 139–152.
- (52) Larkin, J. A. *J. Chem. Thermodyn.* **1975**, *7*, 137–148.
- (53) Turner, J.; Soper, A. K. *J. Chem. Phys.* **1994**, *101*, 6116–6125.
- (54) Petong, P.; Pottel, R.; Kaatz, U. *J. Phys. Chem. A* **2000**, *104*, 7420–7428.
- (55) Onori, G.; Santucci, A. *J. Mol. Liq.* **1996**, *69*, 161–181.
- (56) Ferrario, M.; Haughney, M.; McDonald, I. R.; Klein, M. L. *J. Chem. Phys.* **1990**, *93*, 5156–5166.
- (57) De Loof, H.; Nilsson, L.; Rigler, R. *J. Am. Chem. Soc.* **1992**, *114*, 4028–4035.
- (58) Luzar, A.; Chandler, D. *Nature* **1996**, *379*, 55–57.
- (59) Luzar, A.; Chandler, D. *Phys. Rev. Lett.* **1996**, *76*, 928–931.
- (60) Soper, A. K.; Bruni, F.; Ricci, M. A. *J. Chem. Phys.* **1997**, *106*, 247–254.
- (61) Oleinikova, A.; Brovchenko, I.; Geiger, A.; Guillot, B. *J. Chem. Phys.* **2002**, *117*, 3296–3304.
- (62) Wernet, P.; Nordlund, D.; Bergmann, U.; Cavalleri, M.; Odelius, M.; Ogasawara, H.; Naslund, L. A.; Hirsch, T. K.; Ojamae, L.; Glatzel, P.; Pettersson, L. G. M.; Nilsson, A. *Science* **2004**, *304*, 995–999.
- (63) Kuo, I-F. W.; Mundy, C. J. *Science* **2004**, *303*, 658–660.
- (64) Franks, F.; Ives, P. S. *Q. Rev. Chem. Soc.* **1966**, *20*, 1–44.
- (65) Sato, T.; Buchner, R. *J. Phys. Chem. A* **2004**, *108*, 5007–5015.
- (66) Sato, T.; Chiba, A.; Nozaki, R. *J. Chem. Phys.* **1999**, *2508*–2521.
- (67) Sciortino, F.; Geiger, A.; Stanley, H. E. *Nature* **1991**, *354*, 218–221.
- (68) Stanley, H. E.; Teixeira, J. *J. Chem. Phys.* **1980**, *73*, 3404–3422.
- (69) Lorenz, C. D.; Ziff, R. M. *Phys. Rev. E* **1998**, *57*, 230–236.
- (70) Dougan, L.; Bates, S. P.; Hargreaves, R.; Fox, J. P.; Crain, J.; Finney, J. L.; Réat, V.; Soper, A. K. *J. Chem. Phys.* **2004**, *121*, 6456–6462.
- (71) de Grothuss, C. J. T. *Ann. Chim. (Paris)* **1806**, *LVIII*, 54–74.
- (72) Morrone, J. A.; Tuckerman, M. E. *J. Chem. Phys.* **2002**, *117*, 4403–4413.
- (73) Sprick, M. J. *J. Chem. Phys.* **1991**, *95*, 6762–6769.
- (74) Smith, B. D.; Srivastava, R. *Thermodynamic Data for Pure Compounds*; Elsevier: Amsterdam, 1986.
- (75) Meckl, S.; Zeidler, M. D. *Mol. Phys.* **1988**, *63*, 85–95.
- (76) Eastale, A. J.; Woolf, L. A. *J. Phys. Chem.* **1985**, *89*, 1066–1069.
- (77) Harris, K. R.; Newitt, P. J.; Derlacki, Z. *J. J. Chem. Soc. Faraday Trans.* **1998**, *94*, 1963–1970.